

Article

Water Bodies' Mapping from Sentinel-2 Imagery with Modified Normalized Difference Water Index at 10-m Spatial Resolution Produced by Sharpening the SWIR Band

Yun Du ^{1,*}, Yihang Zhang ^{1,2,3}, Feng Ling ^{1,4}, Qunming Wang ³, Wenbo Li ⁵ and Xiaodong Li ¹

- ¹ Institute of Geodesy and Geophysics, Chinese Academy of Sciences, Wuhan 430077, China; zhangyihang12@mails.ucas.ac.cn (Y.Z.); lingf@whigg.ac.cn (F.L.); lixiaodong@whigg.ac.cn (X.L.)
² University of Chinese Academy of Sciences, Beijing 100049, China
³ Lancaster Environment Center, Faculty of Science and Technology, Lancaster University, Lancaster LA1 4YQ, UK; wqm1111@126.com
⁴ School of Geography, University of Nottingham, University Park, Nottingham NG7 2RD, UK
⁵ Hefei Institute of Technology Innovation, Hefei Institutes of Physical Science, Chinese Academy of Sciences, Hefei 230088, China; wbli@iim.ac.cn
* Correspondence: duyun@whigg.ac.cn; Tel.: +86-27-6888-1352

Academic Editors: Clement Atzberger and Prasad S. Thenkabail

Received: 29 December 2015; Accepted: 18 April 2016; Published: 22 April 2016

Abstract: Monitoring open water bodies accurately is an important and basic application in remote sensing. Various water body mapping approaches have been developed to extract water bodies from multispectral images. The method based on the spectral water index, especially the Modified Normalized Difference Water Index (MNDWI) calculated from the green and Shortwave-Infrared (SWIR) bands, is one of the most popular methods. The recently launched Sentinel-2 satellite can provide fine spatial resolution multispectral images. This new dataset is potentially of important significance for regional water bodies' mapping, due to its free access and frequent revisit capabilities. It is noted that the green and SWIR bands of Sentinel-2 have different spatial resolutions of 10 m and 20 m, respectively. Straightforwardly, MNDWI can be produced from Sentinel-2 at the spatial resolution of 20 m, by upscaling the 10-m green band to 20 m correspondingly. This scheme, however, wastes the detailed information available at the 10-m resolution. In this paper, to take full advantage of the 10-m information provided by Sentinel-2 images, a novel 10-m spatial resolution MNDWI is produced from Sentinel-2 images by downscaling the 20-m resolution SWIR band to 10 m based on pan-sharpening. Four popular pan-sharpening algorithms, including Principle Component Analysis (PCA), Intensity Hue Saturation (IHS), High Pass Filter (HPF) and \AA Trous Wavelet Transform (ATWT), were applied in this study. The performance of the proposed method was assessed experimentally using a Sentinel-2 image located at the Venice coastland. In the experiment, six water indexes, including 10-m NDWI, 20-m MNDWI and 10-m MNDWI, produced by four pan-sharpening algorithms, were compared. Three levels of results, including the sharpened images, the produced MNDWI images and the finally mapped water bodies, were analysed quantitatively. The results showed that MNDWI can enhance water bodies and suppress built-up features more efficiently than NDWI. Moreover, 10-m MNDWIs produced by all four pan-sharpening algorithms can represent more detailed spatial information of water bodies than 20-m MNDWI produced by the original image. Thus, MNDWIs at the 10-m resolution can extract more accurate water body maps than 10-m NDWI and 20-m MNDWI. In addition, although HPF can produce more accurate sharpened images and MNDWI images than the other three benchmark pan-sharpening algorithms, the ATWT algorithm leads to the best 10-m water bodies mapping results. This is no necessary positive connection between the accuracy of the sharpened MNDWI image and the map-level accuracy of the resultant water body maps.

Keywords: remote sensing; Modified Normalized Difference Water Index (MNDWI); Normalized Difference Water Index (NDWI); Sentinel-2; Shortwave-Infrared (SWIR); pan-sharpening; water body mapping

1. Introduction

As an important part of the Earth's water cycle, land surface water bodies, such as rivers, lakes and reservoirs, are irreplaceable for the global ecosystem and climate system. Surveying land surface water bodies and delineating their spatial distribution has a great significance to understanding hydrology processes and managing water resources [1–3]. At present, remote sensing has become a routine approach for land surface water bodies' monitoring, because the acquired data can provide macroscopic, real-time, dynamic and cost-effective information, which is substantially different from conventional *in situ* measurements [4–6]. Various methods, including single band density slicing [7], unsupervised and supervised classification [8–11] and spectral water indexes [12–19], were developed in order to extract water bodies from different remote sensing images. Among all existing water body mapping methods, the spectral water index-based method is a type of reliable method, because it is user friendly, efficient and has low computational cost [20]. Different water indexes have already been proposed in the past few decades. Specifically, McFeeters (1996) proposed the Normalized Difference Water Index (NDWI) [21], using the green and Near Infrared (NIR) bands of remote sensing images based on the phenomenon that the water body has strong absorability and low radiation in the range from visible to infrared wavelengths. NDWI can enhance the water information effectively in most cases, but it is sensitive to built-up land and often results in over-estimated water bodies. To overcome the shortcomings of NDWI, Xu (2006) developed the Modified Normalized Difference Water Index (MNDWI) [22] that uses the Shortwave Infrared (SWIR) band to replace the NIR band used in NDWI. Many previous research works have demonstrated that MNDWI is more suitable to enhance water information and can extract water bodies with greater accuracy than NDWI [12,13,22,23].

In the last few decades, MNDWI had been widely applied to produce water body maps at different scales. In practice, both the spectral information of the SWIR and green bands that are used to calculate MNDWI and the spatial resolutions of both bands directly affect the accuracy of mapped water bodies. For example, MODerate-resolution Imaging Spectroradiometer (MODIS) images have been widely used to map water bodies at both global and regional scales. Specifically, Carroll *et al.* produced a new global raster water mask at 250-m resolution from MODIS dataset [24]. Feng *et al.* used MODIS images between 2000 and 2010 to estimate the inundation changes of Poyang Lake [6]. Huang *et al.* monitored water surface variations using long-term MODIS data time series [25]. For regional studies, images provided by the Thematic Mapper (TM), the Enhanced Thematic Mapper Plus (ETM+) and the latest Operational Land Imager (OLI) from Landsat series satellites are popular datasets. For example, Hui *et al.* modelled the spatial and temporal change of Poyang Lake using multi-temporal Landsat TM and ETM+ images [15]. Du *et al.* extracted the water body maps at subareas over the Yangtze River Basin and Huaihe River Basin in China from Landsat OLI images [13]. Rokni *et al.* extracted water features and detected change using Landsat TM, ETM+ and OLI images [26]. Compared to MODIS, the Landsat TM, ETM+ and OLI images have much finer spatial resolutions (30 m) and can extract open water bodies with more explicit and accurate boundaries. However, the spatial resolution of Landsat series images is still not fine enough to identify smaller-sized open water bodies, such as narrow gutters and small pools in urban areas. By exploring remote sensing images, such as SPOT6/7, IKONOS and Quick-bird, these small-sized water bodies can be mapped. However, these fine spatial resolution images have no SWIR band, making it impossible to use the MNDWI method.

Remarkably, the European Space Agency (ESA) launched a new optical fine spatial resolution satellite, namely Sentinel-2, on 23 June 2015. Sentinel-2 can provide systematic global acquisitions of fine spatial resolution multispectral images with a fine revisit frequency, which is important for the

next generation of operational products, such as land cover maps, land cover change detection maps and geophysical variables [27–29]. The Sentinel-2 images would surely be of great significance for regional water bodies' mapping, due to its appealing properties (*i.e.*, the 10-m spatial resolution for four bands and the 10-day revisit frequency) and the free access. As shown in Table 1, the Sentinel-2 multispectral image has 13 bands in total, in which four bands (blue, green, red and NIR) have a spatial resolution of 10 m and six bands (including SWIR band) have a spatial resolution of 20 m. The MNDWI method can be applied to extract water bodies from the Sentinel-2 images, since the green and SWIR bands are included. However, it is noticed that the spatial resolutions of green and SWIR bands are at 10 m and 20 m, respectively. In this case, it is easy to produce MNDWI with the 20-m resolution, by simply upscaling the green band (Band 3) from 10 m to 20 m. However, spatial information would be lost following this scheme.

Table 1. Band spatial resolution, central wavelength and bandwidth of the Sentinel-2 image.

Band Number	Spatial Resolution (m)	Central Wavelength (nm)	Bandwidth (nm)
B1	60	443	20
B2	10	490	65
B3	10	560	35
B4	10	665	30
B5	20	705	15
B6	20	740	15
B7	20	783	20
B8	10	842	115
B8A	20	865	20
B9	60	945	20
B10	60	1375	30
B11	20	1610	90
B12	20	2190	180

An alternative and advisable way to enhance the performance of water bodies' mapping using the Sentinel-2 imagery is to produce MNDWI at the 10-m resolution by downscaling the SWIR band (Band 11) from 20 m to 10 m. Obviously, the key issue is how to increase the spatial resolution of the SWIR band accurately. In general, spatial interpolation [30,31] and image fusion [32,33] (*e.g.*, pan-sharpening [34]) are the two most popular kinds of methods applied to increase the spatial resolution of remote sensing imagery. The spatial interpolation method is always applied to coarse spatial resolution images directly and does not use any additional datasets. By contrast, image fusion, such as pan-sharpening, is premised on the availability of the fine spatial resolution panchromatic (PAN) band of the same scene and aims to downscale the coarse multispectral imagery to the spatial resolution of the PAN band. Pan-sharpening is widely applied to remote sensing images that have coarse multispectral bands and a fine spatial resolution PAN band, such as MODIS, Landsat TM/ETM+, SPOT, IKONOS and QuickBird imagery. More specifically, image fusion has also been applied widely to produce fine spatial resolution water body maps. For example, Feng *et al.* used the pan-sharpening methods of PCA and IHS to produce the 250-m water body maps by fusing 500-m and 250-m MODIS images to estimate the inundation changes of Poyang Lake [6]. Ashraf *et al.* compared several image fusion methods for the exploring of spectral and spatial information in freshwater environments [32]. Che *et al.* used a nonlinear regression-based fusion method to downscale the MODIS image to improve water body mapping [35]. Wu *et al.* used a statistical regression based image fusion method to downscale the water inundation map from coarse data to fine-scale resolution [36]. In order to produce the 10-m MNDWI from Sentinel-2, only the spatial resolution of the SWIR band needs to be increased. More importantly, Bands 2, 3, 4 and 8 in the Sentinel-2 imagery all have 10-m resolution. Therefore, the 10-m bands in the Sentinel-2 imagery can be treated as PAN-like bands [37,38], and they can provide important fine spatial resolution information to downscale the 20-m bands to 10 m. Motivated by this, in this paper, the pan-sharpening technique was chosen to increase the spatial resolution of SWIR Band

11 to 10 m to match the 10-m green Band 3, using the information provided by directly observed 10-m Bands 2, 3, 4 and 8.

The objectives of this study are to: (1) produce 10-m MNDWI from the Sentinel-2 image by sharpening the SWIR band; (2) compare the performance of various popular pan-sharpening algorithms in producing the 10-m MNDWI; (3) evaluate the performance of the produced 10-m MNDWI in water bodies mapping by comparing it to the 10-m NDWI and the 20-m MNDWI; and (4) explore the relationship between the accuracy of the sharpened SWIR band or the sharpened MNDWI image and the map-level accuracy of the resultant water body map.

2. Study Site and Dataset

The study area in this paper is located at the Venice coastland, Italy. The city of Venice and its lagoon represent an extraordinary environment and human heritage susceptible to loss in surface elevation relative to the mean sea level [39]. The lagoon covers an area of about 550 km² with shallows, tidal flats, salt marshes, islands and a network of channels, which are all sensitive to the changes of surface water bodies. Over the past 100 years, the mean sea level in Venice coastland rose about 23 cm [40], which leads to an obvious expansion of the open water bodies in the Venice coastland and an increase of flooding events, causing great inconvenience for the population and enormous damage to the cultural heritage. Therefore, it is of great interest to extract surface open water bodies and to monitor their changes in the Venice coastland.

The dataset used in this study is the standard Sentinel-2 Level-1C product, which was produced by radiometric and geometric corrections, including ortho-rectification and spatial registration on a global reference system with sub-pixel accuracy. The Sentinel-2 Level-1C product is composed of 100 km × 100 km tiles in the UTM/WGS84 projection and provides the Top-Of-Atmosphere (TOA) reflectance. One scene of the Sentinel-2 Level-1C image acquired on 13 August 2015 (relative orbit: R022) was downloaded from the ESA Sentinel-2 Pre-Operations Hub (<https://scihub.copernicus.eu/>). A subset covering 20 km × 20 km and centered at 45°28'30"N, 12°16'29"E was used for the case study. The false colour composite of the Sentinel-2 image at 10 m is shown in Figure 1a. The study area is mainly covered by open water bodies, urban built-up and vegetation features. The images of the green band at 10 m, the NIR band at 10 m and the SWIR band at 20 m are shown in Figure 1b-d, respectively, and these three bands were involved in the calculation of water indices of NDWI and MNWI.

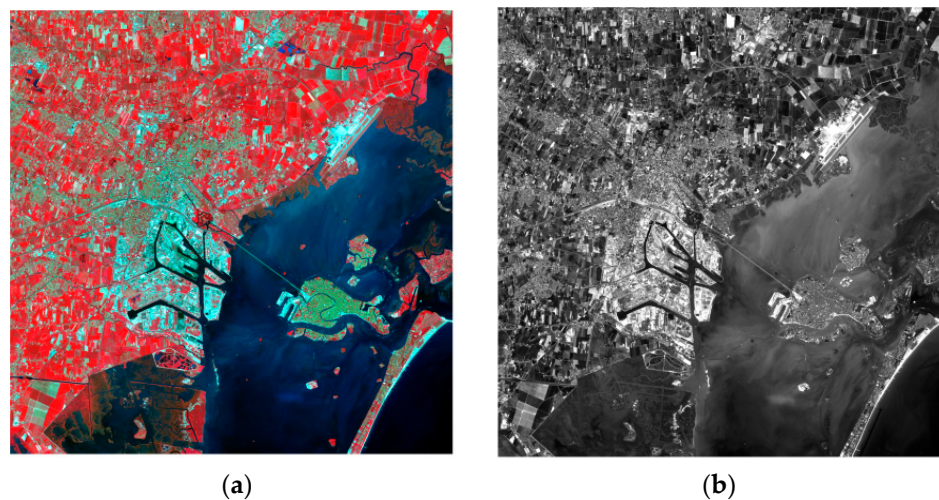


Figure 1. Cont.

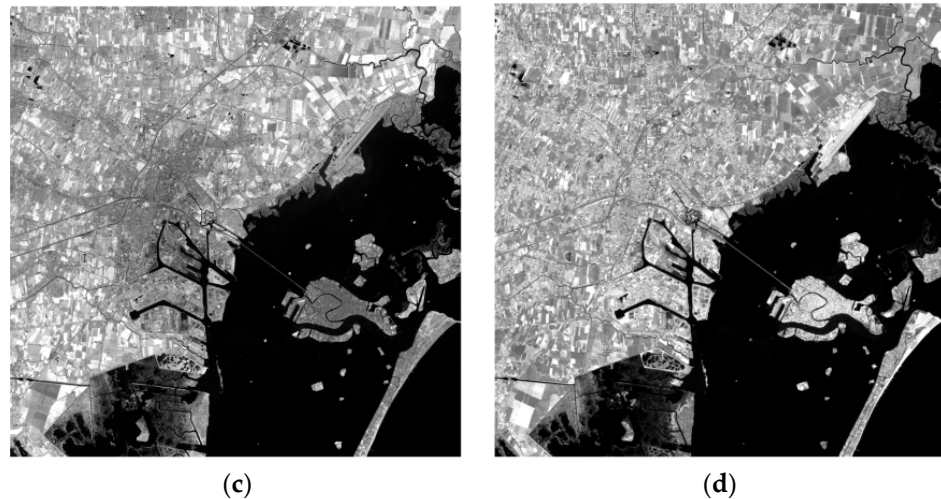


Figure 1. (a) Ten-metre false colour map (R: Band 4; G: Band 3; B: Band 8); (b) 10-m green Band 3; (c) 10-m NIR Band 8; (d) 20-m SWIR Band 11.

3. Methodology

3.1. Spectral Water Indexes

3.1.1. NDWI

The NDWI proposed by McFeeters [21] is designed to: (1) maximize the reflectance of the water body in the green band; (2) minimize the reflectance of water body in the NIR band [22,41]. McFeeters's NDWI is calculated as:

$$\text{NDWI} = \frac{\rho_{\text{Green}} - \rho_{\text{NIR}}}{\rho_{\text{Green}} + \rho_{\text{NIR}}} \quad (1)$$

where ρ_{Green} is the TOA reflectance value of the green band and ρ_{NIR} is the TOA reflectance value of the NIR band. Comparing to the raw Digital Numbers (DN), TOA reflectance is more suitable in calculating NDWI [12,42,43]. The freely-available Sentinel-2 Level-1C dataset is already a standard product of TOA reflectance [27]. Therefore, no additional pre-processing is required, and the NDWI for Sentinel-2 can be directly calculated as:

$$\text{NDWI}_{10m} = \frac{\rho_3 - \rho_8}{\rho_3 + \rho_8} \quad (2)$$

where ρ_3 is the TOA reflectance of the Band 3 (the green band) of Sentinel-2 and ρ_8 is the TOA reflectance of the Band 8 (the NIR band) of Sentinel-2. Note that both Band 3 and Band 8 of Sentinel-2 have the spatial resolution of 10 m, and thus, the calculated NDWI in Equation (2) also has the spatial resolution of 10 m. For clarity, we represent it as NDWI_{10m} .

3.1.2. MNDWI

A main limitation of McFeeters' NDWI is that it cannot suppress the signal noise coming from the land cover features of built-up areas efficiently [22]. Xu [22] noticed that the water body has a stronger absorability in the SWIR band than that in the NIR band, and the built-up class has greater radiation in the SWIR band than that in the NIR band. Based on this finding, the MNDWI was proposed, which is defined as:

$$\text{MNDWI} = \frac{\rho_{\text{Green}} - \rho_{\text{SWIR}}}{\rho_{\text{Green}} + \rho_{\text{SWIR}}} \quad (3)$$

where ρ_{SWIR} is the TOA reflectance of the SWIR band. In general, compared to NDWI, water bodies have greater positive values in MNDWI, because water bodies generally absorb more SWIR light than NIR light; soil, vegetation and built-up classes have smaller negative values, because they reflect more SWIR light than green light [41].

For Sentinel-2, the green band has the spatial resolution of 10 m, while the SWIR band (Band 11) has the spatial resolution of 20 m. Thus, MNDWI needs to be calculated at a spatial resolution of either 10 m or 20 m. The 20-m MNDWI is calculated as:

$$\text{MNDWI}_{20m} = \frac{\rho_3^{20m} - \rho_{11}}{\rho_3^{20m} + \rho_{11}} \quad (4)$$

where ρ_{11} is the TOA reflectance of Band 11 (SWIR) of Sentinel-2 and ρ_3^{20m} is the TOA reflectance of the upscaled Band 3 of Sentinel-2 with a spatial resolution of 20 m. The value of ρ_3^{20m} is calculated as the average value of the corresponding $2 \times 2 \rho_3$ values.

On the other hand, if the spatial resolution of Band 11 is increased from 20 m to 10 m, the MNDWI with the spatial resolution of 10 m, MNDWI_{10m} , can then be calculated as:

$$\text{MNDWI}_{10m} = \frac{\rho_3 - \rho_{11}^{10m}}{\rho_3 + \rho_{11}^{10m}} \quad (5)$$

where ρ_{11}^{10m} refers to the TOA reflectance of Band 11 at 10 m, which is produced by downscaling the original 20-m Band 11. This is achieved by using the pan-sharpening algorithms described in the following.

3.2. Pan-Sharpening Algorithms

In this paper, four popular pan-sharpening algorithms, including PCA [44], IHS [45], *High Pass Filter* (HPF) [46] and *À trous Wavelet Transform* (ATWT) [47] were applied to downscale the Sentinel-2 SWIR band. The basic principles of these different pan-sharpening algorithms are introduced briefly as follows.

3.2.1. PCA

PCA is an approach based on the component substitution for spectral transformation of the original data [48]. Specifically, PCA creates an uncorrelated feature space that can be used as an alternative of the data in the original multispectral feature space. The first Principal Component (PC) image with the largest variance is considered to contain the major information from the original multispectral image, and it is replaced by the fine spatial resolution PAN image [44]. It is noted that before the substitution, the histogram of the PAN image is adjusted to match the first PC. After the substitution, an inverse PC transform is performed to produce the pan-sharpened multispectral image.

3.2.2. IHS

The IHS transform is also a component substitution-based pan-sharpening method. IHS transform separates the spatial information (regarded as intensity) and spectral information (regarded as hue and saturation) into an IHS colour space [45]. The intensity refers to the total brightness of the image, while the hue refers to the dominant or average wavelength of the light contributing to the colour and saturation to the purity of colour. For pan-sharpening, three bands of a multispectral image are first transformed from the RGB domain to the IHS colour space. The PAN component is matched to replace the intensity component of the IHS image, and then, the IHS image is transformed back into the RGB colour space. An improvement model was proposed in [49] to generalize the concept of IHS to multispectral images with more than three bands.

3.2.3. HPF

HPF is a method based on the multi-resolution analysis [34]. The general principle of HPF is to extract high frequency information that is related mostly to the spatial information from the PAN image by using a high pass filter [46]. The high frequency information is then added to each coarse band with a specified weight. Different high pass filters, including the Box filter, Gaussian and Laplacian, can be applied in HPF, and the Box filter is chosen in this paper [46].

3.2.4. ATWT

Similarly to HPF, ATWT is also based on multi-resolution analysis [34]. For ATWT, the original multispectral bands are interpolated to match the spatial resolution of the PAN band. The PAN image and each interpolated band of the multispectral image are decomposed as three high and one low frequency components through wavelet transform. The high frequency component extracted from the PAN image is then merged into the interpolated multispectral bands. Each of the pan-sharpened multispectral bands is finally obtained by the inverse wavelet transform. Three inter-band structure modes, including Context-Based Decision (CBD), Support Value Transform (SVT) and Laplacian pyramids, are widely used in ATWT to rule on the transformation of high frequency components of the PAN image [50], and the Laplacian pyramids are used in this paper.

3.2.5. Algorithm Implementation

As the pan-sharpening algorithm is based on the availability of a PAN or PAN-like band, a suitable PAN-like band needs to be selected from 10-m Bands 2, 3, 4 and 8 at first. In this study, the most suitable PAN-like band was determined by measuring the correlation coefficient between them and the SWIR band. The 10-m band with the greatest correlation coefficient is chosen as the PAN-like band [37,38].

For all four used pan-sharpening algorithms, HPF and ATWT can be applied for coarse multispectral images band by band. To produce the 10-m SWIR band with HPF and ATWT, the 20-m SIWR band can be sharpened using the PAN-like band directly. By contrast, PCA and IHS are based on the component substitution, and multiple coarse bands are required. To facilitate the implemented process, in this study, all six 20-m bands, including Bands 5, 6, 7, 8A, 11 and 12, were used in these pan-sharpening algorithms of PCA, his, HPF and ATWT.

3.3. Water Bodies' Mapping with the OTSU Algorithm

After the NDWI or MNDWI are produced, water bodies can then be mapped by the simple segmentation algorithm using a suitable threshold value. In general, the threshold is often set to be zero in order to map water bodies from NDWI or MNDWI, that is a pixel whose NDWI or MNDWI is larger than zero is considered as water. In practice, however, multispectral images acquired by different satellite platforms at different regions and different times always have different characteristics. Thus, the threshold should be determined according to the feature of water index values themselves in each scene [51]. In this study, the OTSU algorithm [52], a widely-used dynamic threshold method aiming to maximize the inter-class variance, is employed to determine the optimal threshold value t^* for water bodies' mapping with NDWI and MNDWI [12,13].

Assume the NDWI or MNDWI values range from a to b , where $-1 \leq a \leq b \leq 1$. Based on the OTSU algorithm, a threshold value t can divide the NDWI or MNDWI image into two classes: the

non-water class ranging from a to t and the water class ranging from t to b . The optimal threshold value t^* in the OTSU algorithm is determined as follows:

$$\begin{cases} \delta^2 = P_{nw} \cdot (M_{nw} - M)^2 + P_w \cdot (M_w - M)^2 \\ M = P_{nw} \cdot M_{nw} + P_w \cdot M_w \\ P_{nw} + P_w = 1 \\ t^* = \operatorname{Arg} \max_{a \leq t \leq b} \left\{ P_{nw} \cdot (M_{nw} - M)^2 + P_w \cdot (M_w - M)^2 \right\} \end{cases} \quad (6)$$

where δ is the inter-class variance of the non-water class and the water class, P_{nw} and P_w are the possibilities of one pixel belonging to non-water and water, respectively, M_{nw} and M_w are the mean values of the non-water and water classes and M is the mean value of the NDWI or MNDWI image.

3.4. Result Accuracy Assessment

In order to fully assess the performances of different methods, three levels of results, including the sharpened images, the produced MNDWI images and the final mapped water bodies, were analysed with different quantitative indexes, respectively.

The *Quality with No Reference* (QNR) index that is widely used for pan-sharpening quality evaluation without reference data is employed here to assess the sharpening results [34,53]. The QNR index is calculated based on the two terms. One is the spectral distortion index D_λ , which reflects the degree of preserving the spectral information, and the other is the spatial distortion index D_s , which reflects the degree of preserving the spatial details in the PAN band. More precisely, QNR is formulated as:

$$QNR = (1 - D_\lambda)^\alpha (1 - D_s)^\beta \quad (7)$$

where α, β are two weighted coefficients and are typically set to one. The spectral distortion index D_λ and the spatial distortion index D_s are calculated as:

$$D_\lambda = \sqrt[p]{\frac{1}{N(N-1)} \sum_{i=1}^N \sum_{j=1, j \neq i}^N |d_{i,j}(\text{MS}, \text{MS}_f)|^p} \quad (8)$$

$$D_s = \sqrt[q]{\frac{1}{N} \sum_{i=1}^N |Q(\text{MS}_f(i) - \text{P}) - Q(\text{MS}, \text{P}_{LR})|^q} \quad (9)$$

where p and q are weighted coefficients and are typically set to one. N is the number of bands in the observed multispectral image MS, MS_f is the sharpened multispectral image and P_{LR} is upscaled from the observed pan-like band P. The *Q-index* [54] is used here to calculate the dissimilarities between bands, $d_{i,j}(\text{MS}, \text{MS}_f) = Q(\text{MS}(i) - \text{MS}(i)) - Q(\text{MS}_f(i) - \text{MS}_f(i))$.

The value of QNR ranges from 0 to 1, and a higher QNR value indicates a more accurate sharpened result. The QNR index is designed for multiple bands (at least two bands) and cannot be used to validate the sharpened SWIR band solely. Thus, to assess the results produced by different pan-sharpening algorithms, the QNR index was calculated using the SWIR band and Band 8A.

The correlation coefficients (CC) and root-mean-square-error (RMSE) were used to quantitatively compare the four MNDWI_{10m} images produced by four pan-sharpening algorithms. Since the real MNDWI_{10m} image is not available, the MNDWI_{20m} calculated by Equation (4) was used as the reference. The two indexes are calculated as:

$$CC = \frac{\sum_{i=1}^N (\text{MNDWI}_{20m}(i) - \bar{M}_{20m})(\text{MNDWI}_{20m}^{10m\downarrow}(i) - \bar{M}_{20m}^{10m\downarrow})}{\sqrt{\sum_{i=1}^N (\text{MNDWI}_{20m}(i) - \bar{M}_{20m})^2 \cdot \sum_{i=1}^N (\text{MNDWI}_{20m}^{10m\downarrow}(i) - \bar{M}_{20m}^{10m\downarrow})^2}} \quad (10)$$

$$\text{RMSE} = \sqrt{\frac{1}{N} \sum_{i=1}^N (\text{MNDWI}_{20m}(i) - \text{MNDWI}_{20m}^{10m\downarrow}(i))^2} \quad (11)$$

where N is the number of pixels in MNDWI_{20m} , $\text{MNDWI}_{20m}^{10m\downarrow}$ is the MNDWI image at the spatial resolution of 20 m that was generated by upscaling the sharpened MNDWI_{10m} images and \bar{M}_{20m} and $\bar{M}_{20m}^{10m\downarrow}$ are mean values of MNDWI_{20m} and $\text{MNDWI}_{20m}^{10m\downarrow}$, respectively.

To examine the final water body maps produced with different water indexes, map-level accuracy values, including Kappa and Overall Accuracy (OA), as well as class-level accuracy values, including the omission error and the commission error, were employed. The reference water maps were produced by manually digitizing the 10-m false Sentinel-2 image with the help of Google Earth Map. As it is difficult to obtain the reference water body map for the whole study area ($20 \text{ km} \times 20 \text{ km}$) at the spatial resolution of 10 m, the validation of the final water body maps was performed in three separate subareas, with each covering an area of $2 \text{ km} \times 2 \text{ km}$, as shown in Figure 2a.

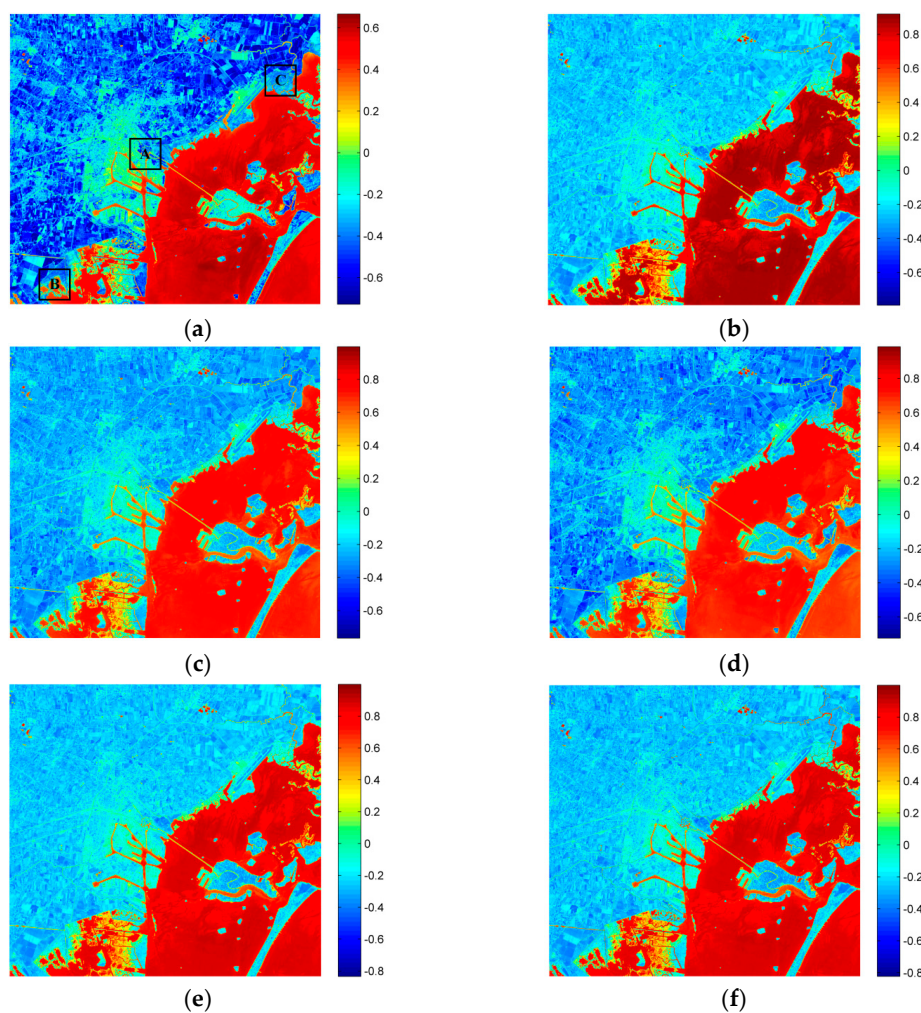


Figure 2. (a) Ten-metre NDWI_{10m} produced by the original green and NIR bands; (b) 20-m MNDWI_{20m} (M, Modified) produced by the upscaled green band and the original SWIR band; (c) 10-m MNDWI_{10m}^{PCA} produced by the original green band and the PCA-sharpened SWIR band; (d) 10-m MNDWI_{10m}^{IHS} produced by the original green band and the his-sharpened SWIR band; (e) 10-m MNDWI_{10m}^{HPF} produced by the original green band and the High Pass Filter (HPF)-sharpened SWIR band; (f) 10-m MNDWI_{10m}^{ATWT} produced by the original green band and the \mathcal{A} Trous Wavelet Transform (ATWT)-sharpened SWIR band. The three black square frames shown in (a) indicate the locations of Subareas A, B and C, respectively.

4. Results and Discussion

4.1. Comparison between NDWI and MNDWI

All six water indexes' images, including NDWI_{10m} , MNDWI_{20m} and four 10-m MNDWI images produced by four pan-sharpening algorithms, $\text{MNDWI}_{10m}^{\text{PCA}}$, $\text{MNDWI}_{10m}^{\text{IHS}}$, $\text{MNDWI}_{10m}^{\text{HPF}}$ and $\text{MNDWI}_{10m}^{\text{ATWT}}$, are shown in Figure 2. All NDWI and MNDWI images clearly enhance the separability of the water bodies. Most MNDWI values of water bodies are larger than 0.8, while most NDWI values of water bodies are larger than 0.5. As shown in Figure 2a, NDWI values of built-up and vegetation are much different. Compared to water bodies, vegetation has much smaller NDWI values, making vegetation easy to distinguish from water bodies. However, built-up features in the NDWI image present in a light yellow tone with positive values between zero and 0.2, especially in the city centres, leading to the confusion between built-up and water bodies. Compared to NDWI, built-up features in the city areas in all MNDWI images present a light cyan tone with values below 0 (Figure 2b–f), indicating that the confusion caused by built-up features in the NDWI image are notably suppressed or even removed in the MNDWI image. This phenomenon agrees with previous research results that MNDWI values of built-up would be smaller than NDWI values, because TOA reflectance values of built-up in the SWIR band are larger than those of NIR.

Table 2 lists the statistical results of water bodies, built-up and vegetation features of Band 3 (green), Band 8 (NIR), Band 11 (SWIR), NDWI and MNDWI images shown in Figure 1b–d and Figure 2a,b, respectively. A similar trend shown in Figure 2 is also found in Table 2. For water bodies, the minimum and maximum values of MNDWI are all larger than those of NDWI. The mean MNDWI value increases by about 0.3 when compared to the mean NDWI value, because the mean TOA value of the SWIR band used for MNDWI is 9.86, while the mean TOA value of the NIR band used for NDWI is 45.75. For built-up features, it is found that the maximum value of NDWI is 0.0845, which is larger than 0. If the threshold value of zero is used to segment water bodies from the NDWI image, some built-up pixels should be wrongly assigned as water. By contrast, the maximum MNDWI value of built-up features is −0.0127, which is much smaller than that of NDWI (0.0845), making built-up features easier to distinguish from water bodies.

Table 2. Maximum (Max), minimum (Min), mean and standard deviation (SD) values of water body, built-up and vegetation features within the Band 3 (green), Band 8 (NIR), Band 11 (SWIR), NDWI_{20m} and MNDWI_{20m} images shown in Figure 1b–d and Figure 2a,b, respectively.

		Green	NIR	SWIR	NDWI_{20m}	MNDWI_{20m}
Water body features	Min	81.7500	22.2500	5.0000	0.3418	0.5920
	Max	121.5000	45.7500	23.0000	0.6000	0.8963
	Mean	105.8400	32.4225	9.8600	0.5296	0.8275
	SD	13.5183	5.1469	4.6035	0.0690	0.0843
Built-up features	Min	108.2500	119.0000	153.0000	−0.2957	−0.3854
	Max	360.7500	398.2500	421.0000	0.0845	−0.0127
	Mean	213.4525	253.1175	292.3300	−0.0829	−0.1626
	SD	63.7689	76.9810	69.9212	0.0737	0.0930
Vegetation features	Min	82.0000	267.7500	127.0000	−0.7117	−0.3766
	Max	109.5000	497.2500	199.0000	−0.4483	−0.1416
	Mean	91.8025	386.6150	158.4300	−0.6058	−0.2632
	SD	7.3246	71.6243	18.7154	0.0798	0.0684

4.2. Comparison between Pan-Sharpening Results

In order to produce NDWI_{10m} , the 20-m SWIR band needs to be sharpened with the pan-sharpening algorithm, by using a suitable PAN-like band to provide detailed spatial information. Figure 3 shows the scatter plots and correction coefficient values between the original 20-m SWIR band

and four upscaled 20-m bands produced from the original 10-m Bands 2, 3, 4 and 8. It is noticed that Band 8 (NIR) has the greatest correction coefficient of 0.8166. Therefore, Band 8 was chosen as the PAN-like band in the pan-sharpening algorithms to produce the 10-m SWIR image.

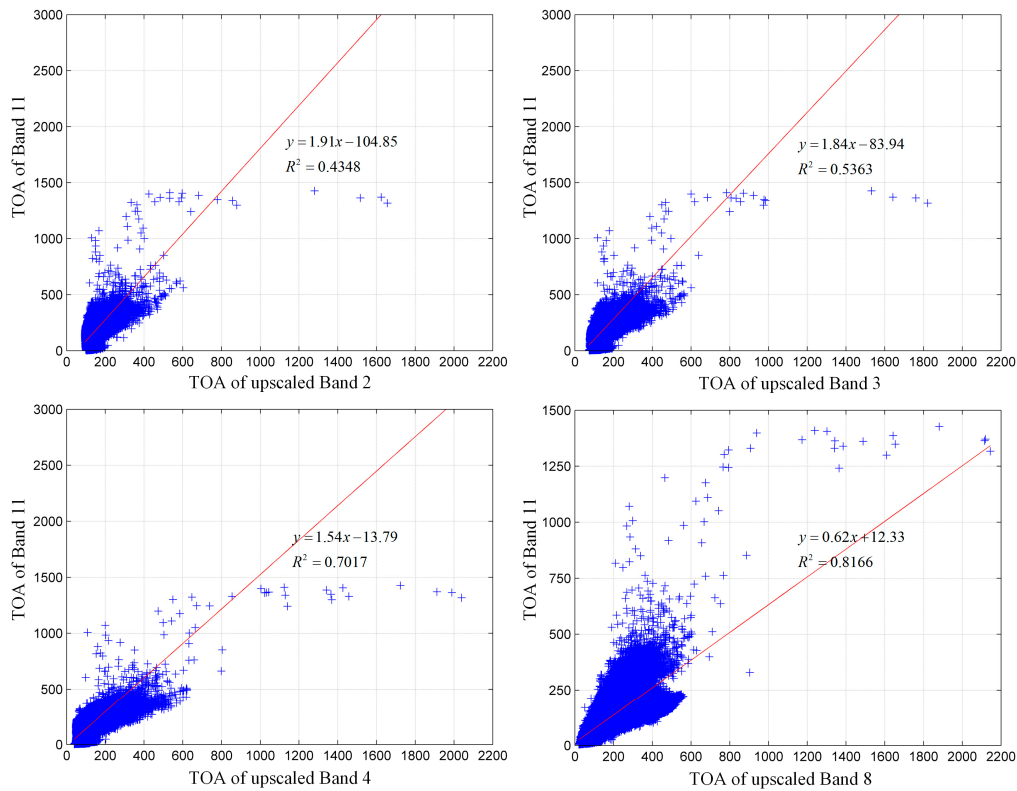


Figure 3. Scatter maps and correlation coefficients between 20-m SWIR band and the four upscaled Bands 2, 3, 4 and 8 of Sentinel-2.

The QNR validation index was used to examine the sharpened SWIR bands with different pan-sharpening algorithms. Table 3 shows the QNR values, including the spectral distortion value D_λ and the spatial distortion value D_s of both sharpened bands (the SWIR band and Band 8A) generated by PCA, IHS, HPF and ATWT, respectively. IHS has the smallest QNR value and the largest D_λ and D_s values, showing that IHS is the weakest algorithm in preserving the spectral information of multispectral bands (20-m SWIR band and Band 8A) and the spatial detail in the PAN band (Band 8). HPF has the smallest D_λ and D_s values of 0.0843 and 0.0626, and the largest QNR value of 0.8584, showing that HPF is more able to preserving the spectral and spatial information of the observed images. Therefore, HPF is considered as the most accurate pan-sharpening algorithm for this case.

Table 3. QNR, D_λ and D_s indexes of the sharpened SWIR band and Band 8A generated by PCA, IHS, HPF and ATWT.

	PCA	IHS	HPF	ATWT
D_λ	0.1258	0.2087	0.0843	0.1342
D_s	0.1428	0.1960	0.0626	0.0872
QNR	0.7494	0.6362	0.8584	0.7902

4.3. Comparison between Different MNDWIs

In Figure 4, enlarged NDWI and MNDWI images of three subareas are shown. It is noticed that there still exists much difference among these images. In general, the spatial resolution is a significant

factor that affects the information of water bodies in the MNDWI image. In the NDWI_{20m} image, many water bodies, especially linear water features, were invisible, and many jagged squares appeared around water boundaries, due to its relatively coarse spatial resolution. By contrast, in all MNDWI_{10m} images, more spatial details of water bodies, especially linear water features, were represented more clearly, and water boundaries become smoother. This is because the sharpened SWIR band, which is used in producing the 10-m MNDWI images, inherited 10-m detailed spatial information from Band 8 (NIR). Visual inspection reveals that PCA- and IHS-based MNDWI images present a dark orange tone that is similar to the 10-m NDWI image, and some water bodies, especially linear water features, are not sufficiently enhanced. This is because the results of PCA and IHS rely heavily on the selected PAN-like band. Since the selected PAN-like band in this study is the 10-m NIR band, the 10-m MNDWI images produced by PCA and IHS are predictably similar to the 10-m NDWI. Compared to PCA and IHS, the ATWT and HPF MNDWI images present a darker red tone that is more similar to the original 20-m MNDWI, and water bodies are all enhanced. This is because HPF and ATWT can preserve more spectral information of the original multispectral image [34].

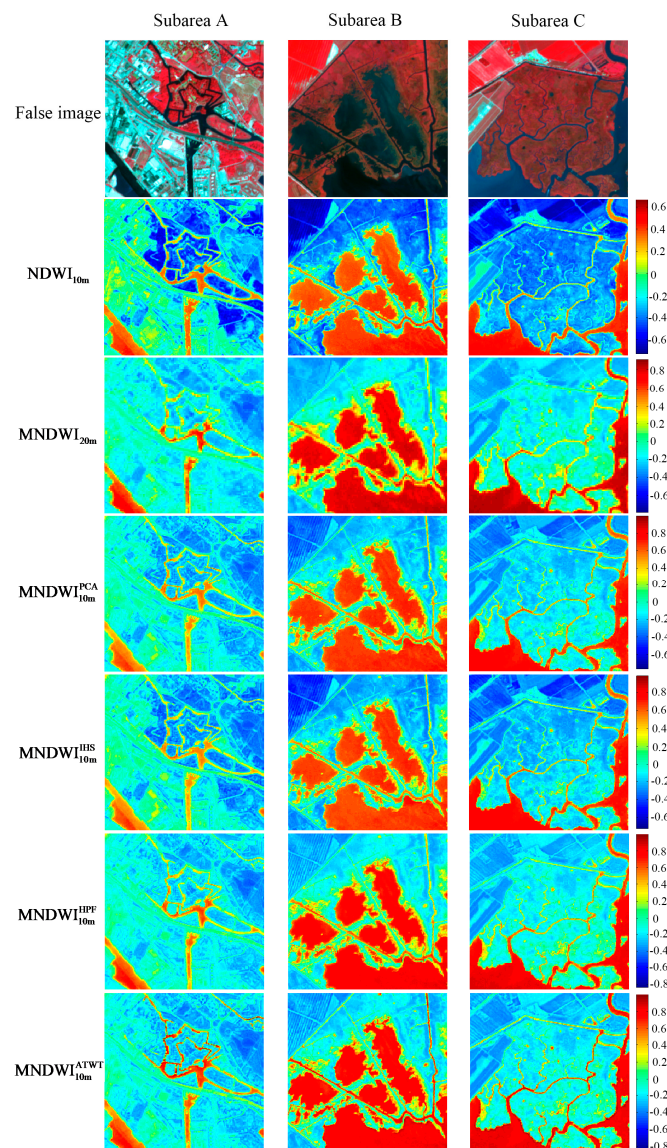


Figure 4. Subarea of the 10-m false colour maps, NDWI and MNDWI images shown in Figures 1 and 2. The first column is for Subarea A; the second column is for Subarea B; and the third column is for Subarea C.

Table 4 shows CC and RMSE values between the original MNDWI_{20m} image and four MNDWI_{20m} images upscaled from the MNDWI_{10m} images produced by PCA, IHS, HPF and ATWT. The trend of CC and RMSE is similar to that of the sharpened band validation result based on the QNR index. The MNDWI image produced by IHS has the smallest CC and the largest RMSE, and HPF produced the largest CC and the smallest RMSE, meaning that HPF has the most satisfactory performance, while IHS has the weakest performance in preserving the information within the observed 20-m MNDWI image.

Table 4. The correlation coefficient (CC) and RMSE between original MNDWI_{20m} image and four upscaled MNDWI_{20m}^{10m↓} images produced by PCA, HIS, HPF and ATWT.

	PCA	IHS	HPF	ATWT
CC	0.9943	0.9862	0.9991	0.9971
RMSE	0.0760	0.1011	0.0215	0.0382

4.4. Comparison between the Resulting Water Body Maps

The final water body maps were extracted by segmenting the NDWI or MNDWI images with the optimal threshold value t^* calculated by the OTSU algorithm. Figure 5 shows the histogram and the corresponding optimal threshold value of each NDWI or MNDWI image. All histograms have bimodal shapes, and optimal threshold values calculated by the OTSU algorithm are all located at the bottoms. In general, the optimal threshold value of NDWI is much smaller than those of MNDWI. The histograms of MNDWI_{20m}, MNDWI_{10m}^{HPF} and MNDWI_{10m}^{ATWT} are similar, and their optimal threshold values are also close. The histogram peak valleys of MNDWI_{10m}^{PCA} and MNDWI_{10m}^{IHS} are narrower, and their optimal threshold values are smaller than those of MNDWI_{10m}^{HPF} and MNDWI_{10m}^{ATWT}.

Three resulting water body maps in different subareas are shown in Figure 6. For the results of NDWI, many isolated pixels (built-up features) are mapped as water bodies, especially in Subarea A. Moreover, many detailed linear water bodies cannot be mapped with NDWI, especially in Subareas B and C. In the water body maps produced by MNDWI_{20m}, most isolated pixels caused by built-up features are eliminated. However, due to the coarse spatial resolution of 20 m, detailed water bodies are still not satisfactorily mapped, and water boundaries are often mapped as jagged squares. For MNDWI_{10m}^{PCA}, isolated pixels in Subarea A caused by built-up features are mostly eliminated; detailed water bodies are satisfactorily mapped, especially in the Subarea C; and water boundaries are smoother than those of MNDWI_{20m}. For MNDWI_{10m}^{IHS}, some isolated pixels caused by built-up features still exist in Subarea A, and the result is similar to those of MNDWI_{10m}^{PCA} in Subareas B and C. For MNDWI_{10m}^{HPF}, linear water bodies are satisfactorily mapped in Subareas B and C, but some linear water bodies are not mapped correctly in Subarea A. Although the 10-m sharpened SWIR band and MNDWI image of HPF are more similar to the observed 20-m SWIR band and MNDWI image than those of ATWT, PCA and IHS, the difference between water body features and non-water body features in the results of HPF is not as obvious as those of ATWT, PCA and IHS. Therefore, HPF often makes a confusion between water and non-water body features, although it can better preserve the information of the observed image. By contrast, in the results of MNDWI_{10m}^{ATWT}, isolated pixels in Subarea A caused by built-up features are almost eliminated completely, and more detailed water bodies are correctly mapped in Subareas B and C, showing the most satisfactory performance of ATWT in producing the 10-m resolution MNDWI for water bodies' mapping. The reason behind this is that ATWT enhances the water body features, especially the linear water body features. Although enhancing water body features makes the resultant pan-sharpened SWIR and corresponding 10-m MNDWI image have a lower accuracy than those of HPF, as shown in Tables 3 and 4 it benefits the water body mapping; because, in this case, water body features become easier to distinguish from non-water body features.

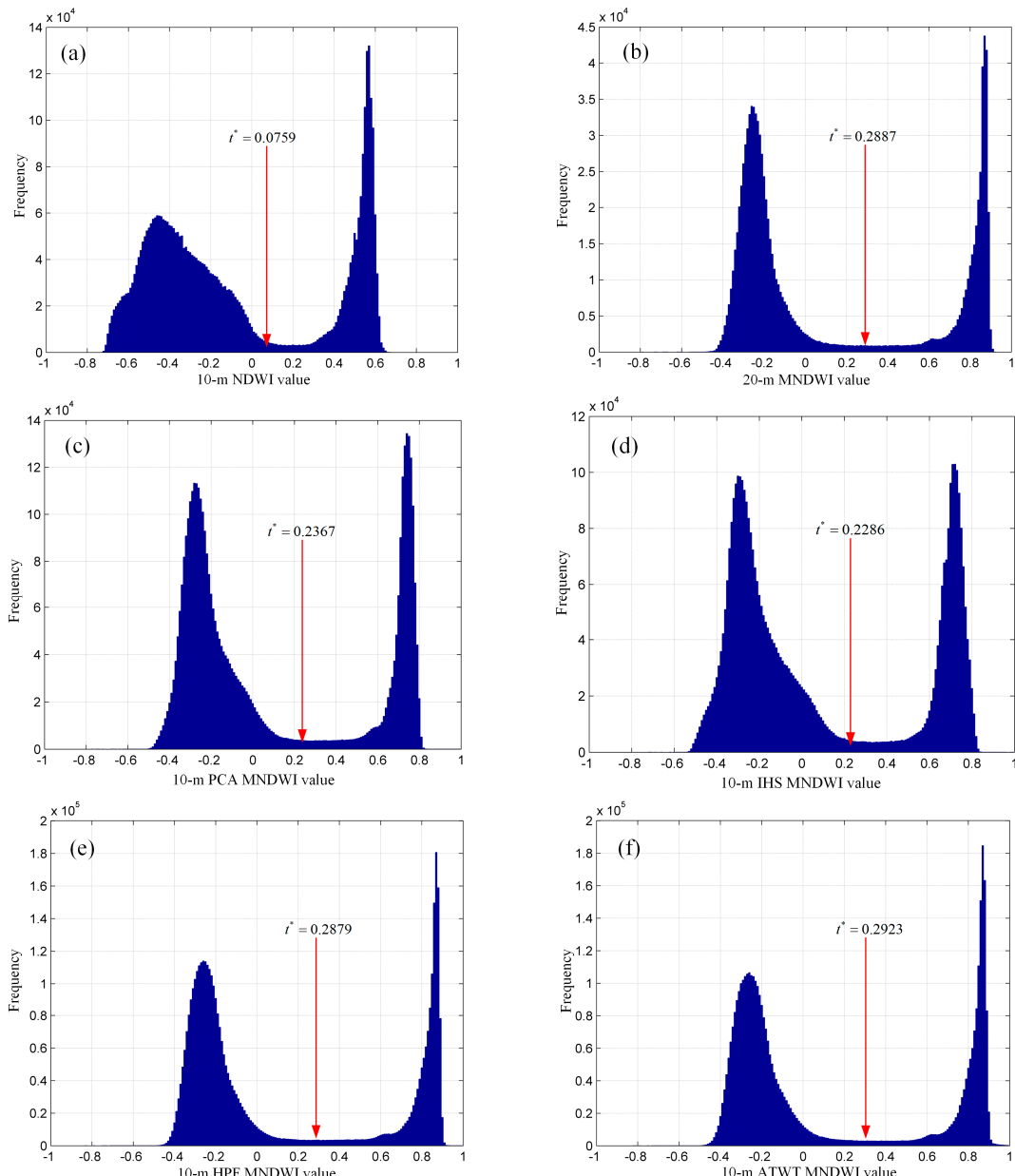


Figure 5. The histograms and optimal threshold values calculated by the OTSU method for the: (a) NDWI_{10m}; (b) MNDWI_{20m}; (c) MNDWI_{10m}^{PCA}; (d) MNDWI_{10m}^{IHS}; (e) MNDWI_{10m}^{HPF}; and (f) MNDWI_{10m}^{ATWT}.

The corresponding statistic accuracies of three different water body maps are shown in Table 5. Water body maps produced by 10-m NDWI images have the smallest average commission errors. When compared to MNDWI_{10m}, however, large average omission errors are also achieved in 10-m NDWI images, because MNDWI is more suitable to enhance the water body features than NDWI. MNDWI_{20m} has the largest average omission error, due to its coarse spatial resolution. Compared to MNDWI_{20m}, the average Kappa values of MNDWI_{10m} produced by PCA, IHS, HPF and ATWT are larger, showing the effectiveness of pan-sharpening for water bodies' mapping. Compared to NDWI, the average Kappa values of MNDWI_{10m} produced by PCA, IHS HPF and ATWT increase by 0.0262, 0.0245, 0.0065 and 0.0338, respectively. This indicates the superiority of MNDWI over NDWI. Although the average commission errors of MNDWI_{10m}^{ATWT} are larger than those of MNDWI_{10m}^{HPF}, MNDWI_{10m}^{PCA} and NDWI, the largest average Kappa and OA values and the smallest average omission error are achieved by MNDWI_{10m}^{ATWT}, suggesting the superiority of ATWT in mapping water bodies.

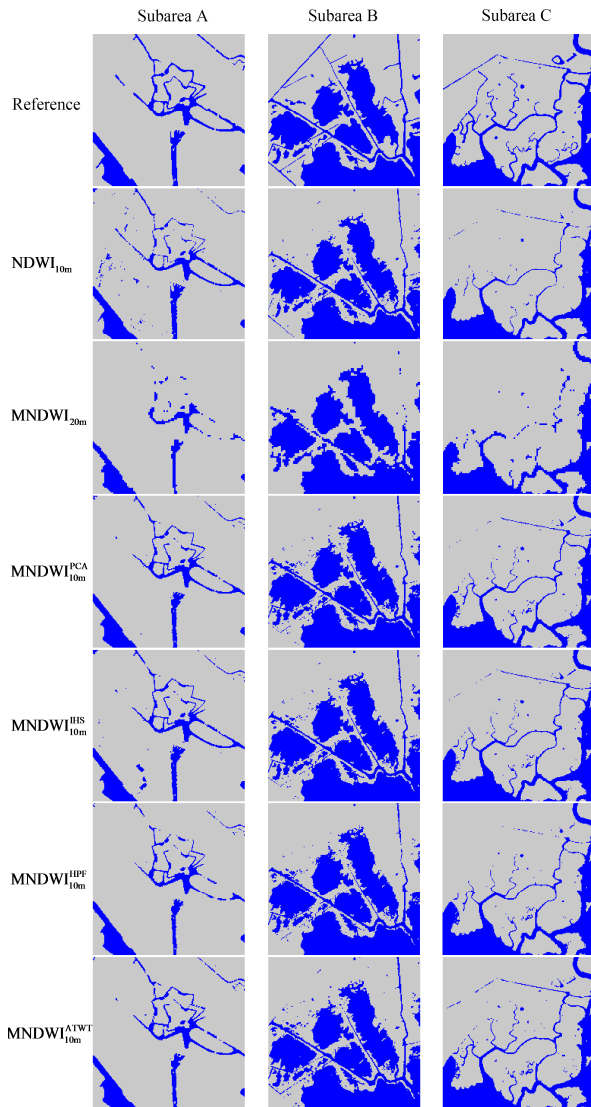


Figure 6. Subarea reference 10-m water body maps and 20-m and 10-m water body maps extracted from the sub-area NDWI and MNDWI images shown in Figure 4.

Table 5. Kappa, Overall Accuracy (OA), omission error and commission error of resultant water body maps in Subareas A, B and C.

	NDWI _{10m}	MNDWI _{20m}	MNDWI _{10mPCA}	MNDWI _{10mHHS}	MNDWI _{10mHPF}	MNDWI _{10mATWT}
Kappa	A	0.8464	0.7037	0.8756	0.8700	0.8334
	B	0.8974	0.8579	0.8955	0.8954	0.8905
	C	0.8435	0.8289	0.8947	0.8952	0.8828
	Average	0.8624	0.7968	0.8886	0.8869	0.8962
OA	A	97.20%	95.36%	97.78%	97.61%	97.13%
	B	95.07%	93.12%	94.92%	94.91%	94.67%
	C	94.86%	94.28%	96.41%	96.44%	96.02%
	Average	95.71%	94.25%	96.37%	96.32%	95.94%
Commission Error	A	8.81%	1.98%	3.30%	7.55%	2.74%
	B	2.53%	7.65%	6.92%	6.87%	6.94%
	C	0.47%	4.71%	2.33%	1.92%	2.88%
	Average	3.94%	4.78%	4.18%	5.45%	4.19%
Omission Error	A	18.29%	42.19%	17.93%	15.43%	24.68%
	B	9.54%	9.05%	5.21%	5.28%	5.81%
	C	21.89%	20.85%	13.48%	13.75%	14.72%
	Average	16.57%	24.03%	12.21%	11.49%	15.07%

4.5. Impact of the Threshold Value on the Performance of Water Mapping

Figure 7 is used here to show how the threshold values affect the performance of water mapping for different NDWI and MNDWI images of different methods. The water mapping threshold value is set to be in the range of zero to 0.4 with an interval of 0.05 by considering the histograms of different NDWI and MNDWI images shown in Figure 5. From Figure 7, it can be found that the optimal threshold value of the NDWI image is in the range of zero to 0.1, while that of MNDWI images are in the range of 0.2 to 0.35, and the optimal threshold values t^* calculated by the OTSU algorithm (see Figure 5) for NDWI and MNDWI images are following these optimal ranges of zero to 0.1 (NDWI) and 0.2 to 0.35 (MDNWI). NDWI is more sensitive to the change of the water mapping threshold value than MDNWI. If the threshold value of NDWI is larger than 0.1, the Kappa values of the resultant water maps will have a severe decrease. Similar trends shown in Table 5 are also found in Figure 7; the $MNDWI_{20m}$ has the lowest Kappa values in the optimal ranges by comparing to other 10-m NDWI and MNDWI images. For the four pan-sharpening-based 10-m MNDWI images, the results of ATWT have the highest Kappa values by comparing to those of PCA, IHS and HPF.

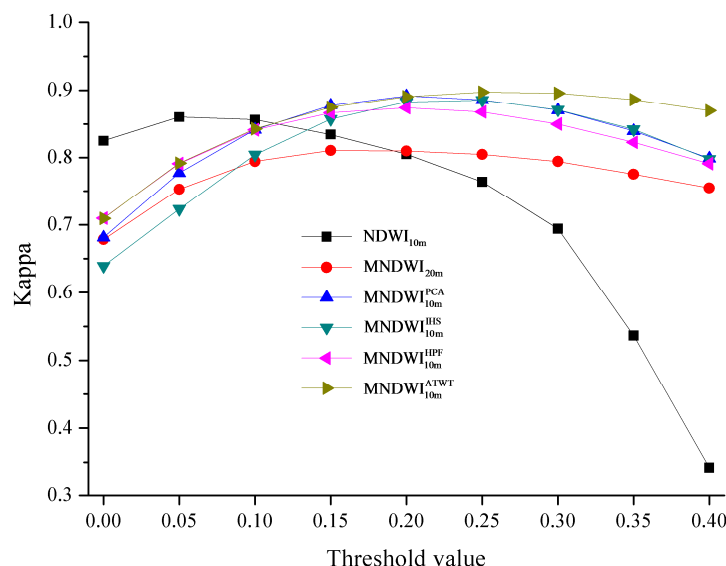


Figure 7. The mean Kappa values of the water maps of Subarea A, B and C produced by different water mapping threshold values (in the range of 0 to 0.4).

5. Conclusions

The newly-launched Sentinel-2 can provide fine spatial resolution multispectral imagery at a fine temporal resolution, which makes it an important dataset for water bodies' mapping at the global scale. In this paper, a novel method is proposed for water bodies' mapping from the Sentinel-2 image by producing the 10-m MNDWI image. In order to take full advantage of the Sentinel-2 image that has four 10-m bands, including green and NIR, and six 20-m bands, including SWIR, pan-sharpening is applied to downscale the 20-m SWIR band to 10 m by using the 10-m NIR band as the PAN-like band. Four popular pan-sharpening algorithms, including PCA, IHS, HPF and ATWT, are compared. The experiment on the subset Sentinel-2 image located at Venice coastland demonstrates that MNDWI is more efficient to enhance water bodies and to suppress built-up features than NDWI. All 10-m MNDWIs produced by PCA, IHS, HPF and ATWT can represent more detailed spatial information of water bodies than 20-m MNDWI. As a result, 10-m MNDWIs can be used to extract more accurate water body maps than 10-m NDWI and 20-m MNDWI. Amongst the four used pan-sharpening algorithms, HPF produces the sharpened 10-m SWIR band with a higher QNR value and the 10-m MNDWI image with a higher correlation coefficient and a lower RMSE by comparing to PCA, IHS and ATWT.

However, HPF makes a confusion between water and non-water body features and cannot produce water body maps with higher accuracy than the other three pan-sharpening algorithms. Compared to PCA, IHS and HPF, ATWT is most likely to enhance water body features (especially the linear water body features) and can produce the most reliable 10-m MNDWI, which yields the most accurate water bodies' maps. In general, this is no necessary positive connection between the accuracy (QNR, CC and RMSE values) of the sharpened SWIR band or the sharpened MNDWI image and the map-level accuracy of the resultant water body map, because the two kinds of accuracies focus on different key points. QNR, CC and RMSE aim to measure the similarity between the sharpened image and the observed coarse image, while map-level accuracy of the resultant water body map mainly focuses on the difference between water body features and non-water features in the NDWI or MNDWI images. In future research, more powerful pan-sharpening algorithms, which can better take into account the characteristics and water body feature and the spectral and spatial features of the Sentinel-2 image will be explored.

Acknowledgments: This work was supported in part by the Natural Science Foundation of Hubei Province for Distinguished Young Scholars under Grant 2013CFA031, by the National Basic Research Program (973 Program) of China under Grant 2013CB733205 and the key project from Institute of Geodesy and Geophysics under Grant Y409123012.

Author Contributions: Yun Du, Yihang Zhang and Feng Ling conceived of the main idea and designed and performed the experiments. Qunming Wang made contributions to the pan-sharpening model. Wenbo Li and Xiaodong Li made contributions to the water index models. The manuscript was written by Yun Du and Yihang Zhang and was improved by the contributions of all of the co-authors.

Conflicts of Interest: The authors declare no conflict of interest.

References

1. Papa, F.; Prigent, C.; Rossow, W.B. Monitoring flood and discharge variations in the large siberian rivers from a multi-satellite technique. *Surv. Geophys.* **2008**, *29*, 297–317. [[CrossRef](#)]
2. Roberts, N.; Taieb, M.; Barker, P.; Damnati, B.; Icole, M.; Williamson, D. Timing of the younger dryas event in east-Africa from lake-level changes. *Nature* **1993**, *366*, 146–148. [[CrossRef](#)]
3. Vorosmarty, C.J.; Sharma, K.P.; Fekete, B.M.; Copeland, A.H.; Holden, J.; Marble, J.; Lough, J.A. The storage and aging of continental runoff in large reservoir systems of the world. *AMBIO* **1997**, *26*, 210–219.
4. Chen, Q.L.; Zhang, Y.Z.; Ekroos, A.; Hallikainen, M. The role of remote sensing technology in the EU water framework directive (WFD). *Environ. Sci. Policy* **2004**, *7*, 267–276. [[CrossRef](#)]
5. Du, Y.; Xue, H.P.; Wu, S.J.; Ling, F.; Xiao, F.; Wei, X.H. Lake area changes in the middle Yangtze region of China over the 20th century. *J. Environ. Manag.* **2011**, *92*, 1248–1255. [[CrossRef](#)] [[PubMed](#)]
6. Feng, L.; Hu, C.M.; Chen, X.L.; Cai, X.B.; Tian, L.Q.; Gan, W.X. Assessment of inundation changes of Poyang Lake using MODIS observations between 2000 and 2010. *Remote Sens. Environ.* **2012**, *121*, 80–92. [[CrossRef](#)]
7. Work, E.A.; Gilmer, D.S. Utilization of satellite data for inventorying prairie ponds and lakes. *Photogramm. Eng. Remote Sens.* **1976**, *42*, 685–694.
8. Sivanpillai, R.; Miller, S.N. Improvements in mapping water bodies using ASTER data. *Ecol. Inform.* **2010**, *5*, 73–78. [[CrossRef](#)]
9. Sheng, Y.W.; Shah, C.A.; Smith, L.C. Automated image registration for hydrologic change detection in the lake-rich Arctic. *IEEE Geosci. Remote Sens. Lett.* **2008**, *5*, 414–418. [[CrossRef](#)]
10. Huang, C.; Chen, Y.; Wu, J.P. DEM-based modification of pixel-swapping algorithm for enhancing floodplain inundation mapping. *Int. J. Remote Sens.* **2014**, *35*, 365–381. [[CrossRef](#)]
11. Huang, C.; Chen, Y.; Wu, J.P. Mapping spatio-temporal flood inundation dynamics at large river basin scale using time-series flow data and MODIS imagery. *Int. J. Appl. Earth Obs. Geoinf.* **2014**, *26*, 350–362. [[CrossRef](#)]
12. Li, W.B.; Du, Z.Q.; Ling, F.; Zhou, D.B.; Wang, H.L.; Gui, Y.M.; Sun, B.Y.; Zhang, X.M. A comparison of land surface water mapping using the normalized difference water index from TM, ETM plus and ALI. *Remote Sens.* **2013**, *5*, 5530–5549. [[CrossRef](#)]
13. Du, Z.Q.; Li, W.B.; Zhou, D.B.; Tian, L.Q.; Ling, F.; Wang, H.L.; Gui, Y.M.; Sun, B.Y. Analysis of Landsat-8 OLI imagery for land surface water mapping. *Remote Sens. Lett.* **2014**, *5*, 672–681. [[CrossRef](#)]

14. Xie, H.; Luo, X.; Xu, X.; Tong, X.H.; Jin, Y.M.; Pan, H.Y.; Zhou, B.Z. New hyperspectral difference water index for the extraction of urban water bodies by the use of airborne hyperspectral images. *J. Appl. Remote Sens.* **2014**, *8*, 085098. [[CrossRef](#)]
15. Hui, F.M.; Xu, B.; Huang, H.B.; Yu, Q.; Gong, P. Modelling spatial-temporal change of Poyang Lake using multitemporal Landsat imagery. *Int. J. Remote Sens.* **2008**, *29*, 5767–5784. [[CrossRef](#)]
16. Jiang, H.; Feng, M.; Zhu, Y.Q.; Lu, N.; Huang, J.X.; Xiao, T. An automated method for extracting rivers and lakes from landsat imagery. *Remote Sens.* **2014**, *6*, 5067–5089. [[CrossRef](#)]
17. Mizuochi, H.; Hiyama, T.; Ohta, T.; Nasahara, K.N. Evaluation of the surface water distribution in north-central namibia based on MODIS and AMSR series. *Remote Sens.* **2014**, *6*, 7660–7682. [[CrossRef](#)]
18. Yao, F.F.; Wang, C.; Dong, D.; Luo, J.C.; Shen, Z.F.; Yang, K.H. High-resolution mapping of urban surface water using ZY-3 multi-spectral imagery. *Remote Sens.* **2015**, *7*, 12336–12355. [[CrossRef](#)]
19. Li, W.; Qin, Y.; Sun, Y.; Huang, H.; Ling, F.; Tian, L.; Ding, Y. Estimating the relationship between dam water level and surface water area for the Danjiangkou Reservoir using Landsat remote sensing images. *Remote Sens. Lett.* **2016**, *7*, 121–130. [[CrossRef](#)]
20. Ryu, J.H.; Won, J.S.; Min, K.D. Waterline extraction from Landsat TM data in a tidal flat—A case study in Gomso Bay, Korea. *Remote Sens. Environ.* **2002**, *83*, 442–456. [[CrossRef](#)]
21. McFeeters, S.K. The use of the normalized difference water index (NDWI) in the delineation of open water features. *Int. J. Remote Sens.* **1996**, *17*, 1425–1432. [[CrossRef](#)]
22. Xu, H.Q. Modification of normalised difference water index (NDWI) to enhance open water features in remotely sensed imagery. *Int. J. Remote Sens.* **2006**, *27*, 3025–3033. [[CrossRef](#)]
23. Singh, K.V.; Setia, R.; Sahoo, S.; Prasad, A.; Pateriya, B. Evaluation of NDWI and MNDWI for assessment of waterlogging by integrating digital elevation model and groundwater level. *Geocarto Int.* **2015**, *30*, 650–661. [[CrossRef](#)]
24. Carroll, M.L.; Townshend, J.R.; DiMiceli, C.M.; Noojipady, P.; Sohlberg, R.A. A new global raster water mask at 250 m resolution. *Int. J. Digit. Earth.* **2009**, *2*, 291–308. [[CrossRef](#)]
25. Huang, S.F.; Li, J.G.; Xu, M. Water surface variations monitoring and flood hazard analysis in Dongting Lake area using long-term Terra/MODIS data time series. *Nat. Hazards* **2012**, *62*, 93–100. [[CrossRef](#)]
26. Rokni, K.; Ahmad, A.; Selamat, A.; Hazini, S. Water feature extraction and change detection using multitemporal landsat imagery. *Remote Sens.* **2014**, *6*, 4173–4189. [[CrossRef](#)]
27. Drusch, M.; Del Bello, U.; Carlier, S.; Colin, O.; Fernandez, V.; Gascon, F.; Hoersch, B.; Isola, C.; Laberinti, P.; Martimort, P.; et al. Sentinel-2: ESA's optical high-resolution mission for GMES operational services. *Remote Sens. Environ.* **2012**, *120*, 25–36. [[CrossRef](#)]
28. Pesaresi, M.; Corbane, C.; Julea, A.; Florczyk, A.; Syrris, V.; Soille, P. Assessment of the Added-Value of Sentinel-2 for Detecting Built-up Areas. *Remote Sens.* **2016**, *8*, 299. [[CrossRef](#)]
29. Immitzer, M.; Vuolo, F.; Atzberger, C. First Experience with Sentinel-2 Data for Crop and Tree Species Classifications in Central Europe. *Remote Sens.* **2016**, *8*, 166. [[CrossRef](#)]
30. Atkinson, P.M. Downscaling in remote sensing. *Int. J. Appl. Earth Obs. Geoinf.* **2013**, *22*, 106–114. [[CrossRef](#)]
31. Atkinson, P.M.; Pardo-Iguzquiza, E.; Chica-Olmo, M. Downscaling cokriging for super-re solution mapping of continua in remotely sensed images. *IEEE Trans. Geosci. Remote Sens.* **2008**, *46*, 573–580. [[CrossRef](#)]
32. Ashraf, S.; Brabyn, L.; Hicks, B.J. Image data fusion for the remote sensing of freshwater environments. *Appl. Geogr.* **2012**, *32*, 619–628. [[CrossRef](#)]
33. Zhang, H.K.K.; Huang, B. A new look at image fusion methods from a bayesian perspective. *Remote Sens.* **2015**, *7*, 6828–6861. [[CrossRef](#)]
34. Vivone, G.; Alparone, L.; Chanussot, J.; Dalla Mura, M.; Garzelli, A.; Licciardi, G.A.; Restaino, R.; Wald, L. A critical comparison among pansharpening algorithms. *IEEE Trans. Geosci. Remote Sens.* **2015**, *53*, 2565–2586. [[CrossRef](#)]
35. Che, X.H.; Feng, M.; Jiang, H.; Song, J.; Jia, B. Downscaling MODIS surface reflectance to improve water body extraction. *Adv. Meteorol.* **2015**, *2015*, 424291. [[CrossRef](#)]
36. Wu, G.P.; Liu, Y.B. Downscaling surface water inundation from coarse data to fine-scale resolution: Methodology and accuracy assessment. *Remote Sens.* **2015**, *7*, 15989–16003. [[CrossRef](#)]
37. Wang, Q.M.; Shi, W.Z.; Atkinson, P.M.; Zhao, Y.L. Downscaling MODIS images with area-to-point regression kriging. *Remote Sens. Environ.* **2015**, *166*, 191–204. [[CrossRef](#)]

38. Wang, Q.M.; Shi, W.Z.; Atkinson, P.M.; Pardo-Iguquiza, E. A new geostatistical solution to remote sensing image downscaling. *IEEE Trans. Geosci. Remote Sens.* **2016**, *54*, 386–396. [[CrossRef](#)]
39. Strozzi, T.; Teatini, P.; Tosi, L. TerraSAR-X reveals the impact of the mobile barrier works on Venice coastline stability. *Remote Sens. Environ.* **2009**, *113*, 2682–2688. [[CrossRef](#)]
40. Tosi, L.; Carbognin, L.; Teatini, P.; Strozzi, T.; Wegmüller, U. Evidence of the present relative land stability of Venice, Italy, from land, sea, and space observations. *Geophys. Res. Lett.* **2002**, *29*, 3-1–3-4. [[CrossRef](#)]
41. Sun, F.D.; Sun, W.X.; Chen, J.; Gong, P. Comparison and improvement of methods for identifying waterbodies in remotely sensed imagery. *Int. J. Remote Sens.* **2012**, *33*, 6854–6875. [[CrossRef](#)]
42. Chander, G.; Markham, B.L.; Helder, D.L. Summary of current radiometric calibration coefficients for Landsat MSS, TM, ETM+, and EO-1 ALI sensors. *Remote Sens. Environ.* **2009**, *113*, 893–903. [[CrossRef](#)]
43. Ko, B.C.; Kim, H.H.; Nam, J.Y. Classification of potential water bodies using landsat 8 OLI and a combination of two boosted random forest classifiers. *Sensors* **2015**, *15*, 13763–13777. [[CrossRef](#)] [[PubMed](#)]
44. Chavez, P.S.; Kwarteng, A.Y. Extracting spectral contrast in landsat thematic mapper image data using selective principal component analysis. *Photogramm. Eng. Remote Sens.* **1989**, *55*, 339–348.
45. Carper, W.J.; Lillesand, T.M.; Kiefer, R.W. The use of intensity-hue-saturation transformations for merging spot panchromatic and multispectral image data. *Photogramm. Eng. Remote Sens.* **1990**, *56*, 459–467.
46. Chavez, P.S.; Sides, S.C.; Anderson, J.A. Comparison of 3 different methods to merge multiresolution and multispectral data—Landsat tm and spot panchromatic. *Photogramm. Eng. Remote Sens.* **1991**, *57*, 295–303.
47. Shensa, M.J. The discrete wavelet transform—Wedding the a trous and mallat algorithms. *IEEE Trans. Signal Process.* **1992**, *40*, 2464–2482. [[CrossRef](#)]
48. Shah, V.P.; Younan, N.H.; King, R.L. An efficient pan-sharpening method via a combined adaptive PCA approach and contourlets. *IEEE Trans. Geosci. Remote Sens.* **2008**, *46*, 1323–1335. [[CrossRef](#)]
49. Huang, P.S.; Tu, T.M. A new look at IHS-like image fusion methods. *Inf. Fusion* **2007**, *8*, 217–218. [[CrossRef](#)]
50. Garzelli, A.; Aiazzi, B.; Alparone, L.; Baronti, S.; Nencini, F. Interband structure modeling for oversampled multiresolution analysis-based Pan-sharpening of very high resolution multispectral images. *Proc. SPIE* **2003**, *5207*, 678–689.
51. Ji, L.; Zhang, L.; Wylie, B. Analysis of dynamic thresholds for the normalized difference water index. *Photogramm. Eng. Remote Sens.* **2009**, *75*, 1307–1317. [[CrossRef](#)]
52. Lin, K.C. On improvement of the computation speed of Otsu's image thresholding. *J. Electron. Imaging* **2005**, *14*, 023011. [[CrossRef](#)]
53. Alparone, L.; Alazzi, B.; Baronti, S.; Garzelli, A.; Nencini, F.; Selva, M. Multispectral and panchromatic data fusion assessment without reference. *Photogramm. Eng. Remote Sens.* **2008**, *74*, 193–200. [[CrossRef](#)]
54. Wang, Z.; Bovik, A.C. A universal image quality index. *IEEE Signal Process. Lett.* **2002**, *9*, 81–84. [[CrossRef](#)]



© 2016 by the authors; licensee MDPI, Basel, Switzerland. This article is an open access article distributed under the terms and conditions of the Creative Commons Attribution (CC-BY) license (<http://creativecommons.org/licenses/by/4.0/>).